

**Physics-Informed Regression Modelling for Vertical Façade Surface Temperature: A Tropical
Case Study on Solar-reflective Material**

Shisheng Chen^{a, b}, Shanshan Tong^{b, *}, Nyuk Hien Wong^b, May Lwin Oo^b, Joie Lim^b, Erna Tan^b, Ruohan Xu^b, Marcel Ignatius^b, Yang He^c

a-School of Architecture and Urban-Rural Planning, Fuzhou University, Fuzhou, PR China, 350108.

b-Department of the Built and Environment, National University of Singapore, 4 Architecture Drive, Singapore, 117566.

c-College of Environmental Science and Engineering, Donghua University, Shanghai, PR China, 201620.

* Corresponding author.

E-mail address: stong@nus.edu.sg (S Tong)

Abstract:

Urban heat islands (UHI) pose a critical challenge in densely populated cities and tropical climates where large amounts of energy are used to meet the cooling demand. To address this, Building and Construction Authority of Singapore provides incentives for passive cooling such as using of solar-reflective material in its Green Mark guidelines. Thus, understanding about its real-world effectiveness in tropical urban environments is required. Previous field evaluations of solar-reflective material have been limited by short monitoring periods, applications to horizontal surfaces in tropical regions, and the absence of physics-constrained regression tools for predicting vertical façade temperatures. This study addressed these gaps using a hybrid modelling framework combining a transient physical model and data driven model through year-long field measurements. Several machine learning algorithms were compared including multiple-linear regression (MLR), random forest regressor (RF), AdaBoost regressor (AB), extreme gradient boosting regressor (XGB), and TabPFN regressor (TPR). The results indicated that the transient physical model overestimated façade temperatures in the lower temperature ranges. The physics-informed MLR achieved best performance with improved accuracy for pre-cool paint ($R^2=0.96$, $RMSE=0.83^\circ C$) and post-cool paint ($R^2=0.95$, $RMSE=0.65^\circ C$) scenarios, reducing RMSE by 26% and 44%, respectively. The hybrid model also effectively predicted hourly heat fluxes revealing substantial reductions in surface temperature and heat storage with increasing albedo. The maximum net heat flux q_{net} was reduced by about 30-65 W/m^2 in the post-cool paint stage (albedo = 0.73) compared to the pre-cool paint stage (albedo = 0.31). As albedo increases from 0.1 to 0.9, the sensitivity analysis predicts that the maximum daytime surface temperature will decrease by about $11^\circ C$ and the peak heat release of the net heat flux will decrease significantly from about 161 W/m^2 to 27 W/m^2 . These findings underscore the effectiveness of physics-informed regression model for vertical façade surface temperature prediction and value of high-albedo surface in minimizing heat absorption and thermal exchange.

Key words: Physics-Informed Regression Model; Vertical Facade Surface Temperature; Solar-reflective; Passive Cooling;

Nomenclature

Symbol	Meaning
UHI	Urban heat islands UHI
RC	Radiative cooling RC
ML	Machine learning
PIML	Physics-informed machine learning
PIRM	Physics-informed regression models
MLR	Multiple-linear regression
RF	Random forest regressor
AB	Adaboost regressor
XGB	Extreme gradient boosting regressor
TPR	TabPFN regressor
RMSE	Root mean squared error
R^2	Coefficient of determination
$q_{solar_{net}}$	Net absorbed solar radiation
q_{conv}	Convective heat loss
q_{cond}	Conductive heat loss
$q_{rad,sky}$	Radiative heat exchange between surface wall and sky
$q_{rad,ground}$	Radiative heat exchange between surface wall and ground surface
q_{net}	Thermal storage
$q_{solar_{net}}$	Net absorbed solar radiation
RH	Relative humidity
S_{global}	Global solar irradiance
V	Wind speed
T_{air}	Dry-bulb air temperature
$T_{s,TC}$	Surface temperature
$T_{s,IR}$	Surface temperature by infrared camera
T_s	Surface temperature at current timestamp
$T_{s_{previous}}$	Surface temperature at previous timestamp
$T_s^{physics}$	Surface temperature simulated by transient physical model
T_c	Correction term of temperature residual
$T_s^{corrected}$	Corrected surface temperature based on hybrid approach
T_{wall}	Inner wall temperature
T_{sky}	Sky temperature
T_{ground}	Ground surface temperature
α	Albedo
ϵ_{wall}	Emissivity
Bi	Represents the Biot number
h	Convective heat transfer coefficient of air
k	Thermal conductivity of the wall
L	Characteristic length of the geometry
α	Wall surface albedo
G	Total solar irradiance on the façade surface
h_{conv}	Convective heat transfer coefficient of air
h_{cond}	Conductive heat transfer coefficient of wall
ϵ_{sky}	Emissivity of sky;
ϵ_{wall}	Emissivity of wall surface
σ	Stefan-Boltzmann constant
C	Specific heat of wall material
ρ	Density of wall material,

L_{wall}	Thickness of the wall
dT	Change in surface temperature
dt	Time interval

1. Introduction

Urban heat islands (UHI) is one of the most pressing challenges in urban environments requiring immediate attention. The main causes of the UHI effect are the heat release from energy consumption, the heat storage effect of building materials, less surface evaporation from the reduction of green and water spaces, and heat accumulation due to densely clustered buildings [1]. In a tropical city-state such as Singapore, known for its hot and humid climate, the excessive building energy consumption for air conditioning places a significant burden on both city administrators and residents. To mitigate this issue, Building Construction Authority of Singapore has implemented green building design guidelines to improve building energy efficiency. One of the most promising passive cooling strategies for Singapore is cool paints with high solar reflectance index, which has been recommended by the BCA Green Mark 2021 with award for applied area higher than 50% site coverage [1].

1.1 Radiative cooling application in built environment

Traditional radiative cooling (RC) leverages the atmospheric window (8–13 μm) to dissipate heat into outer space providing a sustainable solution to reduce building energy consumption and urban heat accumulation [2,3]. As material science advances, RC materials have evolved and can be classified based on their functions, such as selective emitting materials, reflective materials, back-mirror materials, matrix materials, insulation materials, and dynamic switch layers [2]. Nowadays, RC can provide 24-hour cooling performance through two key mechanisms: (1) high thermal emissivity in the infrared spectrum to maximize emission of longwave radiation [4]; (2) high solar reflectivity (albedo) to minimize heat gain of solar radiation [2]. Increased albedo allows surface to reflect solar radiation directly leading to reduction of radiation heat gain and cooling demand during the daytime and enhanced emissivity enables materials to emit longwave radiation into the sky at night therefore reducing nighttime cooling demand.

The application of RC in buildings has shown significant energy and cost savings in the field measurement. A research in tropical and subtropical climates reported 20–40% reductions in cooling loads over a 20-year lifecycle, alongside lowered global warming potential due to decreased energy-related CO₂ emissions [5]. Another research focused on the impact of super-cool roofs on the overall thermal transfer value finding that super-cool roofs could significantly reduce roof heat gains (73.9 % to 90.7 %) leading to substantial energy savings and cost reductions [6]. RC film applied to a large commercial warehouse reported a 44.36% decrease in daily cooling electricity consumption compared to a conventional steel roof, and calibrated simulation indicated up to 65.2% annual cooling energy savings in different hot climate locations [7]. Mathematical modelling based on physical laws predicted

RC can save up to 25% of cooling energy consumption with an average cooling power of 43–45 W/m² in tropical climate [8]. The cooling benefits of RC modelled at a city scale were reported to be 1.5 °C lower at night and 7.7 °C lower during the day than a concrete roof, with a maximum temperature difference of 15.5 °C at 13:00 [9]. The research also indicated that carbon emission reduced by 0.52 gCO₂/(m²·h) and 0.16 gCO₂/(m²·h) from the applied roof and walls, respectively. While there are many studies on cool roof applications, few studies have explored RC on vertical facades of buildings. Full-scale experiments of RC technology were conducted on prefabricated residential buildings in subtropical climate [10]. The results indicated that roofs coated with RC materials performed far better than façades. Under natural conditions, roofs achieved 132.96% higher daytime and 75.28% higher nighttime cooling relative to white putty, while façades showed only 13.30% and -47.5% during daytime and nighttime, respectively. Under operation of air conditioning, roof benefits remained substantial, with 55.51% improvement during the day and 28.31% at night, whereas façade gains were minimal at 3.58% during the day and negative at -139.13% at night. These results highlight the strong influence of view factor on cooling performance, with vertical façades exhibiting significantly lower cooling potential than horizontal roofs.

1.2 Predicting thermal performance of building envelope

Building thermal performance assessments rely on either physics-based simulations or data driven approaches. Physics-based simulations are theoretically rigorous but computationally expensive when simulating complex urban environments with coupled heat transfer mechanisms at different temporal and spatial scales. In contrast, data driven models excel at data learning but face fundamental limitations in generalization relying on large and high-quality datasets and lack interpretability due to their black-box nature. Combining these two approaches can provide unique solutions for site-specific building applications.

Physics-informed machine learning (PIML) has emerged as a powerful model for solving complex scientific and engineering problems governed by differential equations and physical laws integrating the predictive power of machine learning with the rigor of physics-based modelling [11]. By embedding physical information directly into the neural network architecture via a physics-informed loss function or a hybrid modelling approach, PIML provides accurate and generalizable solutions even with sparse or noisy data. This approach has demonstrated success across diverse domains, including computational fluid dynamics solving Navier-Stokes equations more efficiently than traditional numerical methods [12,13]. Furthermore, the PIML framework was proposed to optimize HVAC systems by embedding physical simulations into data-driven models, thereby achieving optimum controls of thermal comfort, indoor air quality, and cooling loads [14–18]. Traditional building thermal modelling relies on either white box physical model or black box data-driven approaches. Physical models such as EnergyPlus or

CFD are accurate but require detailed inputs which are computationally expensive and difficult to calibrate. Data-driven models such as neural networks are flexible and efficient, but they are prone to overfitting and can produce physically inconsistent predictions. Urban scale applications of such hybrid modelling approaches are diverse and increasingly critical in addressing complex environmental challenges. These include the simulation of land surface temperature for heat island studies [19], urban flood modelling for improved hazard prediction and planning [20], and weather and climate modelling with enhanced spatiotemporal prediction and generalization [21]. However, despite its growing use in urban scale environmental modelling, this approach has not yet been applied to the prediction of vertical façade surface temperature which is a critical variable in surface thermal assessments and building energy performance analysis.

1.3 Research gap and objectives

This research investigated the application of solar-reflective radiative cooling materials on an institutional building in Singapore. The building was selected due to the excessive daytime commercial air-conditioning operations and the building owner's specific interest in reducing peak cooling loads. The vertical façade surface temperature was measured with thermocouple and infrared camera, and surrounding environment conditions were acquired through a mobile weather station. The performance of solar-reflective material involves heat transfer between building and surroundings via radiation, conduction, and convection on the vertical façade of buildings governed by the laws of thermodynamics. Although simulation tools such as like EnergyPlus or CFD can simulate façade temperatures with high physical accuracy, they demand extensive input data (e.g., accurate boundary conditions, detailed 3D building information, thermal and construction properties, computational resources, and calibration effort making them impractical for large-scale or long-term studies. In contrast, solar irradiance simulations on building facade are relatively simple and computationally efficient but translating irradiance data into accurate facade temperature remains a methodological challenge due to the complex coupling of heat transfer mechanisms. This research addressed this gap by developing a PIML model linking solar radiation inputs to façade thermal responses, ensuring physical consistency while substantially improving computational efficiency.

This research hypothesized that the transient physical model offered an approximation of façade temperature, while regression modelling leveraged field measurements to correct and align predictions with observed data. By combining these two data sources, physics-informed regression models (PIRM) were established to enhance the accuracy of vertical surface temperature predictions.

The objectives of this research were: (1) to develop a computationally efficiently and generalized model for vertical façade surface temperature prediction; (2) to evaluate the cooling performance of solar-reflective material on vertical façade. The remaining contents are organized as follows: (1) Section 2 describes the research design, data collection, and modelling methods for vertical facade temperature;

(2) Section 3 presents the experimental results, the differences between transient physical modelling and physics-informed data-driven modelling, and the effect of albedo on facade surface temperature; (3) Section 4 and Section 5 discusses and concludes the limitations of traditional transient physical modelling and the advantages of PIRM in predicting vertical façade surface temperature.

2. Methodology

2.1 Research Design

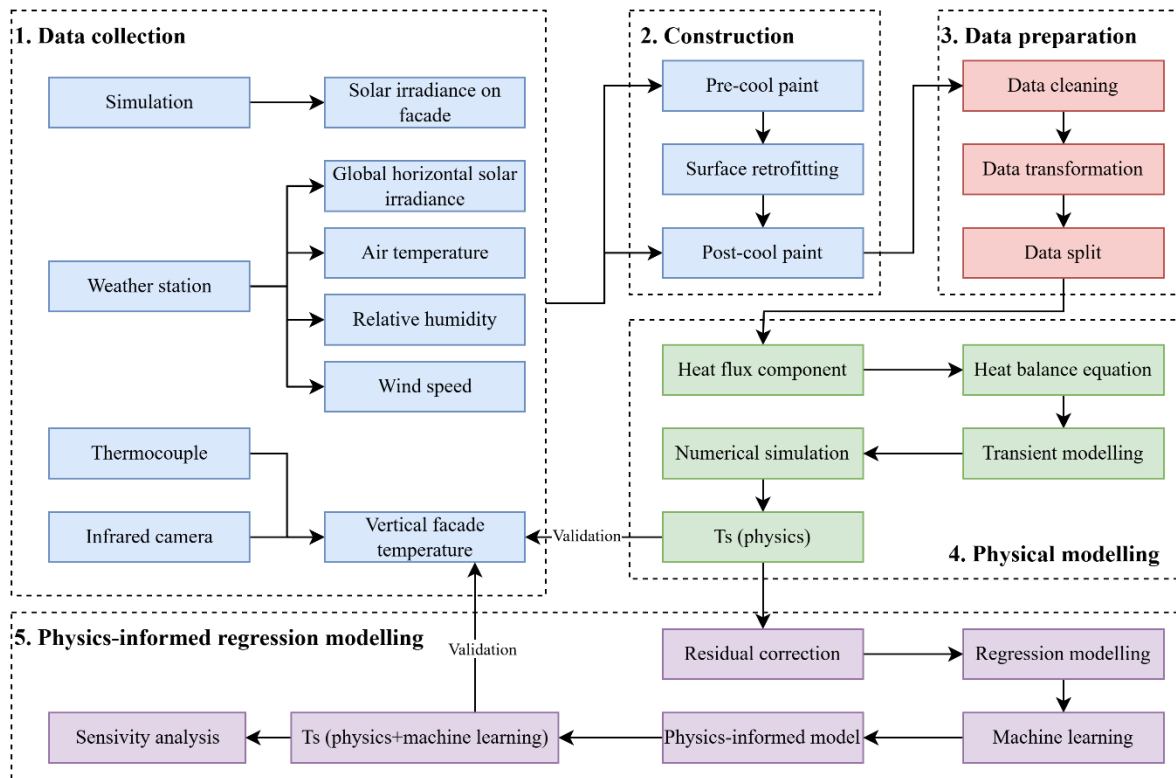


Figure 1: Research design

The research design illustrated in the Figure 1 was structured into five phases including data collection, construction, data preparation, physical modelling and physics informed regression modelling. The initial phase involved gathering continuous data from multiple sources for pre-cool paint and post-cool paint construction, respectively. This included utilizing solar radiation simulation based on Grasshopper Ladybug to model the incoming solar radiation on vertical facade. In addition, a weather station was employed to collect real-time environmental data such as global horizontal solar irradiance, air temperature, relative humidity, and wind speed. To measure the vertical facade temperature, thermocouple wire and an infrared camera were installed to capture thermal images of the facade. This data collection ensured a thorough understanding of the environmental factors influencing the facade's thermal behavior.

Following the data collection and construction, data preparation was implemented to prepare the collected data for detailed analysis. This included data cleaning to remove any noise or irrelevant data

points ensuring the quality of the dataset. Data transformation was then performed to convert the data into a tabular format for analysis. The data was split into training and validation sets for model development.

Subsequently, the heat flux component was analysed to understand the heat transfer through the surface. The heat balance equation was applied to understand the overall heat transfer within the system, and transient modelling was used to analyse the time-varying behaviour of the system. Numerical simulation technique was employed to model the thermal behaviour of the painted surfaces, and experimental results were used to validate the transient physical modelling results. This phase was pivotal in understanding the physics behind the vertical façade heat transfer.

Regression modelling and machine learning techniques were employed to develop predictive models to enhance the accuracy of physical modelling. Residual correction was applied to adjust the model for any discrepancies between predicted and observed values. Another validation step was applied to compare the results between physics-informed modelling and experiments. Furthermore, a sensitivity analysis of the vertical façade surface temperature at different surface albedo was performed to understand the thermal behaviour of the solar-reflective cool paint. The hourly-average of measured air temperature, relative humidity, wind speed and simulated incoming solar radiation on the vertical facade were used in sensitivity analysis in Section 3.3.

2.2 Data collection and analysis

A field experiment was conducted on the west-facing vertical façade of an institutional building in Singapore from January 1st to November 30th, 2024, with the exception of a two-week period from July 14th to 27th, 2024, during which cool paint was applied. The solar-reflective cool paint from Nippon Paint (SolarReflect Linen White) was applied on the exterior façade surface to increase its albedo (solar reflectance) from 0.31 to 0.73, while the emissivity remained unchanged at 0.95, based on on-site measurement using reflectometer and emissometer. The wall is made of 150 mm brick, 12 mm external cement plaster, and 12 mm internal gypsum. The wall material properties were summarised in Table 1.

Table 1: Material properties of wall

Material properties	Value
Albedo of wall surface (pre-cool paint)	0.31
Albedo of wall surface (post-cool paint)	0.73
Emissivity of wall surface	0.95
Thermal conductivity of wall (brick wall)	0.94 W/m·K
Conductive heat transfer coefficient of wall (brick wall)	5.41 W/m ² ·K
Thickness of wall (150 mm brick wall + 12 mm cement plaster + 12 mm gypsum plaster)	0.174 m
Specific heat of wall material (brick wall)	840 J/kg·K
Density of wall material (brick wall)	1650 kg/m ³

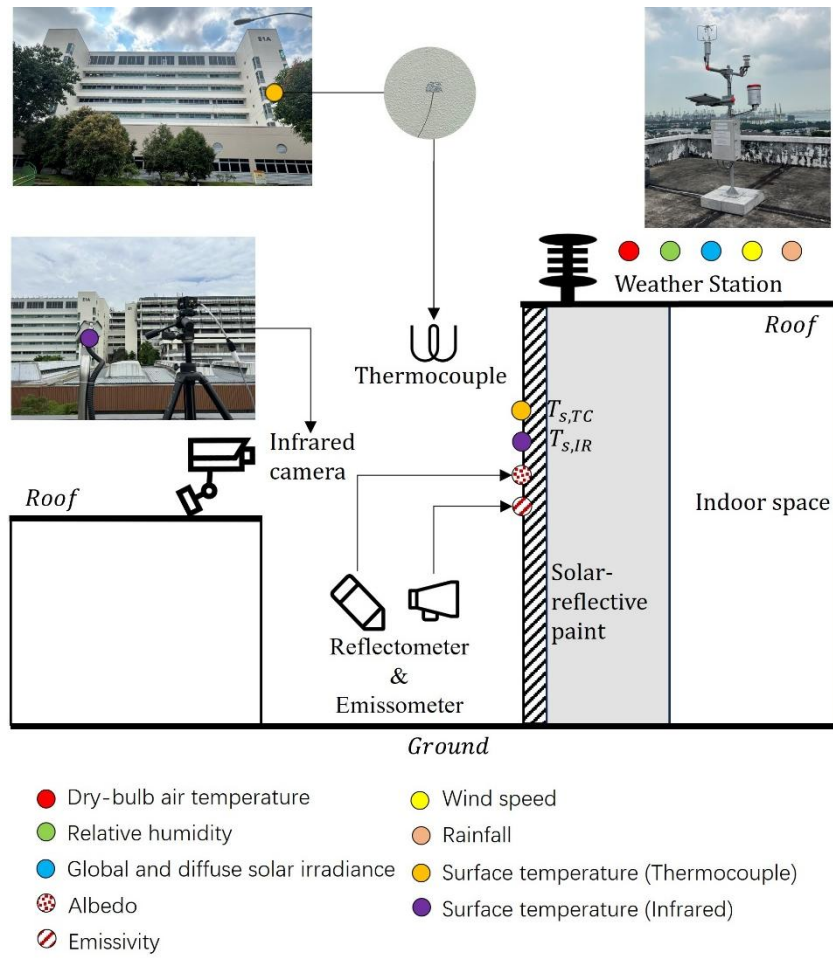


Figure 2: The schematic of data collection

As shown in Figure 2, the exterior façade surface temperature of the studied building was recorded continuously using FLIR A50 infrared camera at 30-min interval. Thermocouple was also installed on the exterior surface of the naturally ventilated staircase lobby for calibration purpose recording data at 1-min interval. A weather station was installed on the building rooftop to collect ambient environmental conditions at 1-min interval, including the dry-bulb air temperature, relative humidity, global solar irradiance, wind speed and rainfall. The data was subsequently resampled and merged based on the timestamp of data collected from infrared camera. The specifications of sensors and equipment used in the field measurement were listed in Table 2.

Table 2: Specification of sensors and equipment

Parameter	Sensor/Equipment	Measurement Range	Accuracy	Resolution
Dry-bulb air temperature (T_{air})	LSI temperature/RH Thermohygrometer	-50°C-100°C	±0.1°C	0.01°C

Relative humidity (RH)	LSI temperature/RH Thermohygrometer	0-100%	1%	0.1%
Global solar irradiance (S_{global})	Delta-T Devices SPN1 Sunshine pyranometer	0-2000 W/m ²	±5%	0.6 W/m ²
Wind speed (V)	LSI 3-axis ultrasonic anemometers DNB200	0-60 m/s	±0.2 m/s	0.01 m/s
Rainfall	Ultrasonic anemometers	0-500 mm/h	±0.2 mm	0.2 mm
Surface temperature ($T_{s,TC}$)	Type-T thermocouple wires	0-370 °C	±0.51°C	0.1°C
Surface temperature by infrared camera ($T_{s,IR}$)	FLIR A50 smart sensor camera	-20 to 175°C	±2°C	N/A
Albedo (α)	Surface Optics 410-solar reflectometer	0-1	±0.02±0.03	N/A
Emissivity (ϵ_{wall})	AZ Technology SRI 1000 portable emissometer	3um to 35um	±2%	N/A

The data collection periods for pre-cool paint and post-cool paint were from 2024 Jan 1st to 2024 July 14th and 2024 July 27th to 2024 Nov 30th, respectively. The rooftop weather data was collected and processed to select the typical hot days for further analysis. The selected days satisfy the following criteria:

- Total rain = 0 mm
- Diurnal air temperature profile is bell-curved.
- Daily max global radiation is higher than 800 W/m².

In total, 14 days of pre-cool paint and 18 days of post-cool paint were selected for the model training and test. The hourly solar irradiance on the vertical building façade during the selected 32 typical hot days were modelled by Radiance and Grasshopper based on the 3D model of studied building, with the measured global and diffuse solar irradiance on the rooftop as input.

2.2 Heat Balance of Vertical Façade

As illustrated in Figure 3, the vertical facade temperature (T_s) of a building was determined through a heat balance model that accounts for incident solar radiation, convective and conductive heat transfer, longwave radiative exchange. The average Bi number calculated from Equation (1) was 2.05 larger than 0.1 suggesting that internal temperature gradient within the wall cannot be ignored. Nevertheless, this study did not aim to resolve the internal temperature field of the wall. In contrast, the external surface temperature was the primary target of this study which was the key performance indicator for solar-reflective coatings. Therefore, the vertical wall was modelled using lumped capacitance method

validated through field measurement with R^2 of 0.86-0.93 for predicting the external wall surface temperature.

$$Bi = \frac{hL}{k} \quad (1)$$

Where Bi represents the Biot number; h = convective heat transfer coefficient of air, $W/m^2 \cdot K$; k = thermal conductivity of the wall, $0.94 W/m \cdot K$; L = characteristic length of the geometry, $0.087m$.

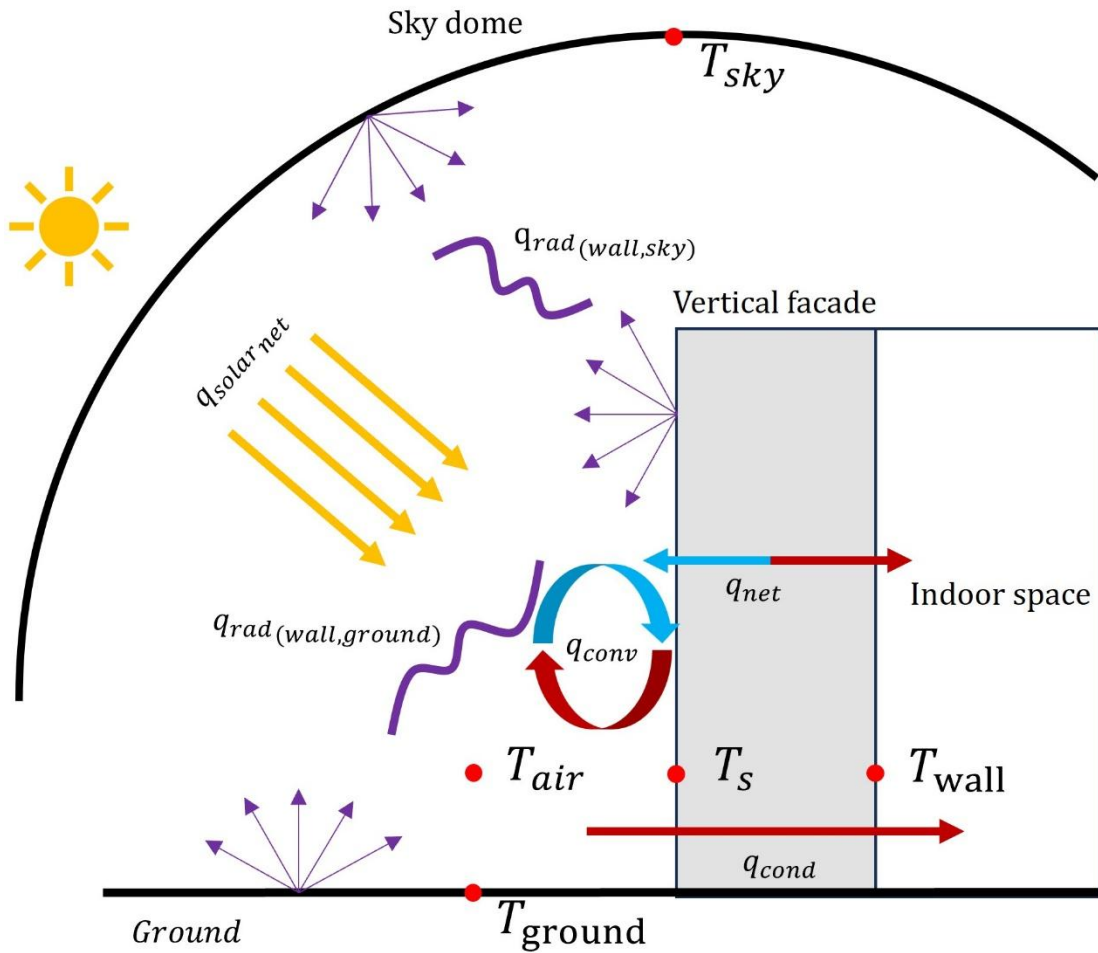


Figure 3: The schematic of the heat balance of vertical facade

(1) Surface Energy Balance

The governing equation (Equation (2)) was derived from the principle of energy conservation at the façade surface to determine how much heat was retained within the system.

$$q_{solar_{net}} - q_{conv} - q_{rad,sky} - q_{rad,ground} - q_{cond} = q_{net} \quad (2)$$

Where $q_{solar_{net}}$ = net absorbed solar radiation, W/m^2 ; q_{conv} = convective heat loss, W/m^2 ; q_{cond} = conductive heat loss, W/m^2 ; $q_{rad,sky}$ = radiative heat exchange between surface wall and sky, W/m^2 ;

$q_{rad,ground}$ = radiative heat exchange between surface wall and ground surface, W/m²; q_{net} = thermal storage, W/m².

(2) *Net absorbed solar irradiance*

$$q_{solar_{net}} = (1 - \alpha) \cdot G \quad (3)$$

Where $q_{solar_{net}}$ = net absorbed solar radiation, W/m²; α = wall surface albedo;

G = total solar irradiance on the façade surface, W/m².

(3) *Convective Heat Transfer*

The convective heat flux represented the heat transfer between surface and surrounding air (Equation (4)). The convective heat transfer coefficient h_{conv} was empirically determined from wind speed (V) using the relation in Equation (5) [22,23]:

$$q_{conv} = h_{conv} \cdot (T_s - T_{air}) \quad (4)$$

$$h_{conv} = 10.45 - V + 10 \cdot V^{0.5} \quad (5)$$

Where q_{conv} = convective heat loss, W/m²; h_{conv} = convective heat transfer coefficient of air, W/m²·K; V = wind speed, m/s; T_{air} = air temperature, °C; T_s = surface temperature at current timestamp, °C.

(4) *Conductive Heat Transfer*

The conductive heat flux through the wall was modelled using Equation (6), where inner wall temperature was assumed to be the air temperature as the experiment was conducted in natural ventilated space:

$$q_{cond} = h_{cond} \cdot (T_s - T_{wall}) \quad (6)$$

Where q_{cond} = conductive heat loss, W/m²; h_{cond} = conductive heat transfer coefficient of wall, 5.41 W/m²·K; T_s = surface temperature at current timestamp, °C; T_{wall} : inner wall temperature, °C.

(5) *Radiative Heat Exchange*

Longwave radiation exchange between vertical facade with the sky and ground followed the Stefan-Boltzmann law:

$$q_{rad,sky} = \varepsilon_{wall} \cdot \sigma \cdot \left((T_s + 273.15)^4 - (T_{sky} + 273.15)^4 \right) \quad (7)$$

$$q_{rad,ground} = \varepsilon_{wall} \cdot \sigma \cdot \left((T_s + 273.15)^4 - (T_{ground} + 273.15)^4 \right) \quad (8)$$

The wall and sky emissivity were treated as constant. The sky emissivity was estimated using an empirical correlation based on dew point temperature (T_{dp}) in Equation (9) [24]:

$$\varepsilon_{sky} = 0.711 + 0.56 \cdot \left(\frac{T_{dp}}{100}\right) + 0.73 \cdot \left(\frac{T_{dp}}{100}\right)^2 \quad (9)$$

The dew point temperature (T_{dp}) was calculated from air temperature (T_{air}) and relative humidity (RH) using Equation (10) [24]:

$$T_{dp} = \frac{234.04 \cdot \left[\ln\left(\frac{RH}{100}\right) + \frac{17.625 \cdot T_{air}}{234.04 + T_{air}}\right]}{17.625 - \ln\left(\frac{RH}{100}\right) - \frac{17.625 \cdot T_{air}}{234.04 + T_{air}}} \quad (10)$$

The sky temperature was then computed using Equation (11) [25,26] :

$$T_{sky} = T_{air} \cdot \varepsilon_{sky}^{0.25} \quad (11)$$

Where $q_{rad,sky}$ = radiative heat exchange between surface wall and sky, W/m²; $q_{rad,ground}$ = radiative heat exchange between surface wall and ground surface, W/m²; ε_{sky} = emissivity of sky; ε_{wall} = emissivity of wall surface, 0.95; σ = Stefan-Boltzmann constant, 5.67e-8 W/m²·K⁴; T_s = surface temperature at current timestamp, °C; T_{sky} = sky temperature, °C; T_{ground} = ground surface temperature, °C; RH = relative humidity, %.

$$q_{rad_{net}} = q_{solar_{net}} - q_{rad,sky} - q_{rad,ground} \quad (12)$$

Where $q_{rad_{net}}$ =net radiation heat flux, W/m²; $q_{solar_{net}}$ = net absorbed solar radiation, W/m²; $q_{rad,sky}$ = radiative heat exchange between surface wall and sky, W/m²; $q_{rad,ground}$ = radiative heat exchange between surface wall and ground surface, W/m²;

(6) Net heat flux

q_{net} represented the amount of heat retained in the facade system as determined by the previous equations. It was used to solve Equation (13) for the change in vertical facade temperature (dT), which was a function of the specific heat of the wall material, the mass per unit area of the wall material, and the change in wall surface temperature.

$$q_{net} = C \cdot \rho \cdot L_{wall} \cdot \frac{dT}{dt} = C \cdot \rho \cdot L_{wall} \cdot \frac{T_s - T_{s_{previous}}}{dt} \quad (13)$$

Where q_{net} = net heat flux, W/m²; C = specific heat of wall material, 840 J/kg·K; ρ = density of wall material, 1650 kg/m³; L_{wall} = thickness of the wall, 0.174 m; dT = change in surface temperature, °C; dt = time interval, s; T_s = surface temperature at current timestamp, °C; $T_{s_{previous}}$ = surface temperature at previous timestamp, °C.

2.3 Physics-Based Vertical Facade Temperature Model with Residual Correction

This model predicted surface temperature by combining a first principles heat transfer model with a data-driven correction term. The governing equations balanced the heat transfer components to estimate the surface temperature at each time step. However, this transient physical model could produce systematic residuals due to unmodeled effects (e.g., paint aging, shading, sensor uncertainties). To

address this, an additional machine-learned correction term (T_c) was introduced as showed in the Equation (14). This correction term captured the difference between the predicted and true surface temperature modelled using a regressor based on features including G , T_{air} , RH , and V in Equation (15).

$$T_s^{corrected} = T_s^{physics} + T_c \quad (14)$$

$$T_c = f(G, T_{air}, RH, V) \quad (15)$$

Where $T_s^{corrected}$ = corrected surface temperature based on hybrid approach, °C; $T_s^{physics}$ = surface temperature simulated by transient physical model, °C; T_c =correction term of temperature residual, °C; G = total solar irradiance on the façade surface, W/m²; T_{air} = air temperature, °C; RH = relative humidity, %; V = wind speed, m/s;

This hybrid approach leveraged full advantage of the interpretability of physical model and the flexibility of machine learning to improve prediction accuracy under different environmental conditions and surface treatments.

2.4 Settings of Machine Learning Algorithms

The training, testing and validation of machine learning (ML) algorithms were executed using Python version 3.9 [27]. Since modelling vertical surface temperature with residual correction is a supervised regression task, it was addressed using several machine learning models including multiple-linear regression (MLR), random forest regressor (RF), AdaBoost regressor (AB), extreme gradient boosting regressor (XGB), and TabPFN regressor (TPR). These algorithms represent a range of ensemble learning and meta learning approaches.

MLR was modelled using “sklearn.linear_model.LinearRegression” [28]. RF was implemented using “sklearn.ensemble.RandomForestRegressor” [28]. AB is an ensemble learning method that sequentially combines weak estimators to form a strong estimator, implemented based on “sklearn.ensemble.AdaBoostRegressor” [28]. XGB is an advanced implementation of gradient boosting designed for speed and performance, incorporating regularization and handling missing data efficiently[29]. XGB was implemented using “xgboost 3.0.0” Python library. TabPFN stands for Tabular Prior-Data Fitted Network, leverages a foundation of synthetic prior data generated using structural causal models [30]. Millions of synthetic datasets capture diverse tabular relationships and serve as prior knowledge. When new tabular data (with N samples and D features) is introduced, it is processed using a transformer architecture pre-equipped with this prior knowledge. The model interprets this data through a piecewise constant distribution framework for regression tasks and outputs both predictions and associated uncertainty estimations. This design enables highly efficient and accurate modeling, especially for small datasets. The model was implemented using the Python library “tabpfn 2.0.8” [30].

For hyperparameters optimization, a Bayesian optimization with 5-fold cross-validation was implemented for RF, XGB and AB. As shown in Table 3, RF was optimized for max depth, min sample split and number of estimators. AB was optimized for learning rate and number of estimators. while XGB was optimized for learning rate, max depth, and number of estimators. MLR and TPR were trained with their default settings which did not require any tuning during training.

To assess the predictive performance of various models, evaluation was conducted using unseen data. For the physics-based model developed without any data fitting, the entire dataset was used for evaluation. In contrast, the physical model with residual term was trained based on machine learning. In order to ensure the generalization of the proposed model on limited data, a 5-fold cross-validation was applied. In addition, a separate validation set comprising both pre-cool and post-cool paint data was used to assess model performance. The evaluation was performed bidirectionally. In the first scenario, the pre-cool paint data was used for training while the post-cool paint data served as the validation set. In the second scenario, the roles were reversed, with the post-cool paint data used for training and the pre-cool paint data used for validation. The physical model was used as a benchmark to compare the prediction performance between different models.

Table 3: Settings of hyperparameters optimization

Model	Hyperparameter	Optimized range
RF	n_estimators	Integer (50, 300)
	max_depth	Integer (5, 20)
	min_samples_split	Integer (2, 20)
	min_samples_leaf	Integer (1, 20)
AB	n_estimators	Integer (50, 300)
	learning_rate	Real number (0.01, 0.2)
XGB	n_estimators	Integer (50, 300),
	max_depth	Integer (3, 15)
	learning_rate	Real number (0.01, 0.2)
	subsample	Real number (0.5, 1.0)

This research employed root mean squared error (RMSE) and the coefficient of determination (R^2) as performance metric. In contrast to the mean squared error, RMSE (Equation 16) gives an error measurement in the same units as the dependent variable and imposes a stricter penalty on large errors compared to the mean absolute error. R^2 (Equation 17) represents the proportion of the variance in the dependent variable predictable from the independent variables.

$$\text{RMSE} = \sqrt{\frac{1}{n} \sum_{i=1}^n (Y_i - \hat{Y}_i)^2} \quad (16)$$

where n is the number of observations, Y_i is a given observation and \hat{Y}_i is the predicted value.

$$R^2 = 1 - \frac{\sum_{i=1}^n (Y_i - \hat{Y}_i)^2}{\sum_{i=1}^n (Y_i - \bar{Y})^2} \quad (17)$$

where n is the number of observations; Y_i is a given observation; \hat{Y}_i is the predicted value and \bar{Y} is the average observation value.

3. Results

3.1 Ambient weather conditions

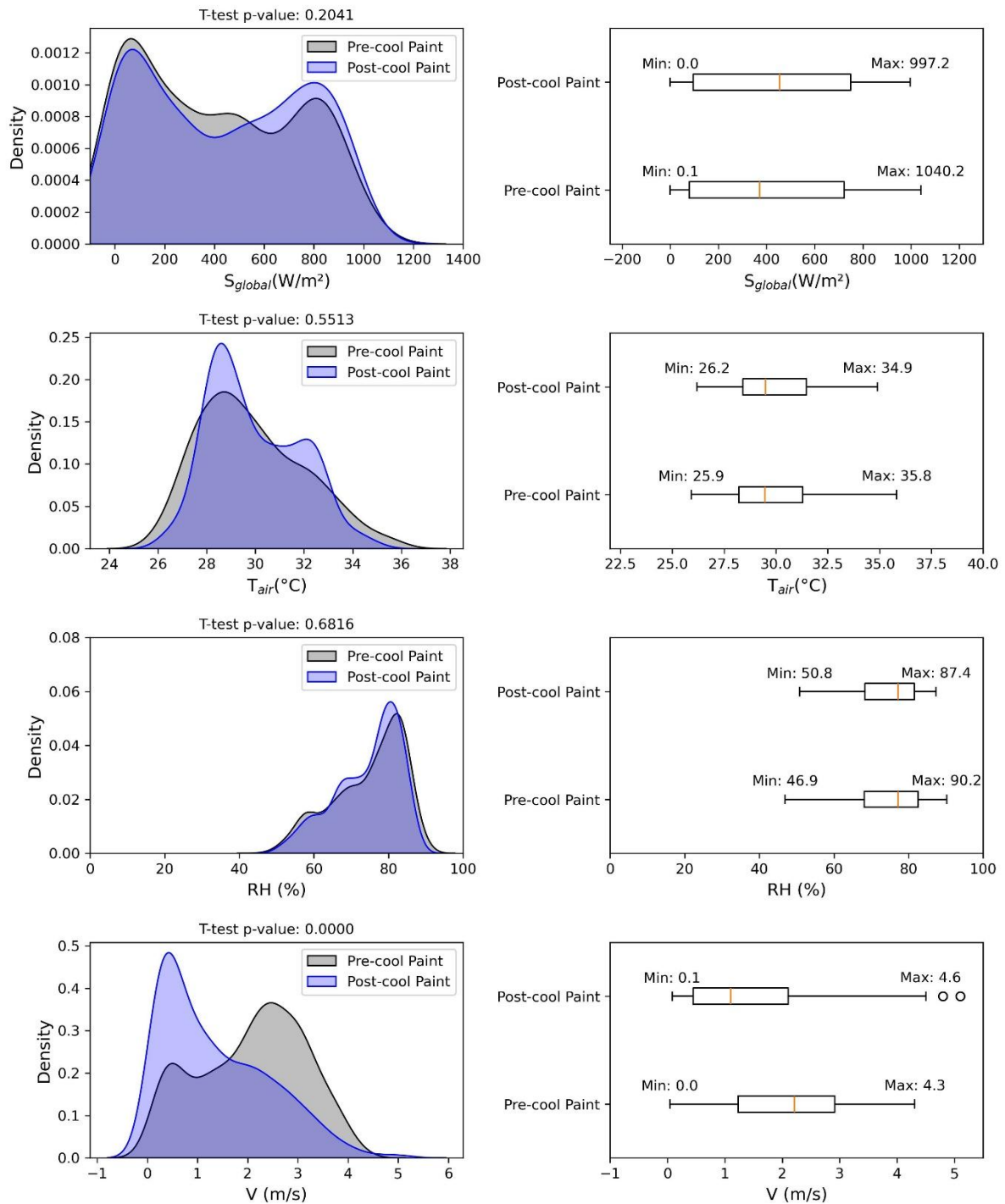


Figure 4: Weather profile during the experiment period

The weather profile data presented in the Figure 4 and Table 4 revealed changes in S_{global} , T_{air} , RH and V during the pre-cool paint and post-cool paint period, respectively. The ambient environmental conditions of S_{global} , T_{air} , and RH were almost identical (T-test p-value >0.05) during the pre-cool paint and post-cool paint period, ensuring consistent test conditions for the comparative experiments.

The maximum S_{global} for post-cool paint was 997.2 W/m² slightly lower than the pre-cool paint maximum of 1040.2 W/m². The maximum T_{air} for post-cool paint was 34.9°C slightly lower than the pre-cool paint maximum of 35.8°C. The maximum RH for post-cool paint was 90.2% slightly higher than the pre-cool paint maximum of 87.4%. In terms of V , the 75th percentile wind speed values during pre-cool paint and post-cool paint periods were less than 3 m/s, meeting the selection criteria of clear, hot, and calm weather in Singapore in tropical climate [31]. The maximum V for post-cool paint was 4.6 m/s slightly higher than the pre-cool paint maximum of 4.3 m/s.

Table 4: Environmental conditions

Statistics	S_{global}		T_{air}		RH		V	
	Pre-cool Paint	Post-cool Paint	Pre-cool Paint	Post-cool Paint	Pre-cool Paint	Post-cool Paint	Pre-cool Paint	Post-cool Paint
mean	408.9	437.8	29.8	29.9	74.6	74.4	2.1	1.4
std	319.8	325.1	2.2	1.9	9.5	8.7	1.1	1.1
min	0.1	0.0	25.9	26.2	46.9	50.8	0.0	0.1
25%	78.7	96.0	28.2	28.4	68.1	68.4	1.2	0.4
50%	370.8	454.7	29.5	29.5	77.2	77.2	2.2	1.1
75%	723.6	749.2	31.3	31.5	82.5	81.5	2.9	2.1
max	1040.2	997.2	35.8	34.9	90.2	87.4	4.3	5.1

3.2 Comparisons of vertical surface temperature predictions

Table 5 illustrates the model performance for predicting vertical façade temperature. Overall, physics alone underestimated post-cool paint effects on vertical façade temperature while physics model with ML correction reduced the prediction errors.

Table 5: Model performance for predicting vertical façade temperature

Phase	Model	Training RMSE	Training R ²	Test RMSE	Test R ²
Pre-cool paint	Physics	N/A	N/A	1.12	0.92
	Physics + MLR	0.60	0.96	0.83	0.96
	Physics + RF	0.37	0.98	0.86	0.95
	Physics + AB	0.48	0.97	0.85	0.95
	Physics + XGB	0.38	0.98	0.85	0.95
	Physics + TPR	0.33	0.99	0.86	0.95
Post-cool paint	Physics	N/A	N/A	1.17	0.84
	Physics + MLR	0.80	0.96	0.65	0.95
	Physics + RF	0.61	0.98	0.68	0.95
	Physics + AB	0.67	0.97	0.69	0.94
	Physics + XGB	0.64	0.97	0.66	0.95
	Physics + TPR	0.39	0.99	0.77	0.93

Figure 5 illustrates the analysis of predicted vertical façade surface temperature by transient physical model. It was evident from time series plot that the physical model's agreement with the ground truth data varied across different temperature ranges. In both pre-cool paint and post-cool paint scenario, the model predictions closely followed the ground truth during periods of higher temperatures indicating a strong agreement in capturing the fluctuations and trends. However, the model showed a noticeable deviation from the ground truth in the lower temperature range suggesting the model was inaccurate in capturing the nighttime surface temperature fluctuations.

The scatter plots compared the predicted temperature against the ground truth. For the pre-cool paint condition, the points were tightly clustered around the line of $y=x$ indicating a high degree of correlation ($R^2 = 0.92$) and a low RMSE of 1.12°C . In contrast, the post-cool paint condition showed a slightly lower correlation ($R^2 = 0.84$) and a higher RMSE of 1.17°C due to the altered thermal properties of the façade, which was not fully captured by the model.

The density plots of residuals provided insights into the distribution of the differences between the predicted and actual temperatures. In the pre-cool paint scenario, the density plot shows a normal distribution centred at a mean residual of -0.56°C , with most residuals falling within ± 1 standard deviation. This suggested that the transient physical model slightly overestimated the temperatures. In the post-cool paint scenario, the density plot had a mean residual of -0.77°C indicating a greater tendency to overestimate temperatures and a higher variability in the model's predictions.

Overall, the transient physical model overestimated the vertical façade surface temperature especially in lower temperature range and change of façade thermal properties also introduced additional uncertainties into the model's predictions requiring potential adjustments to improve accuracy in specific temperature ranges.

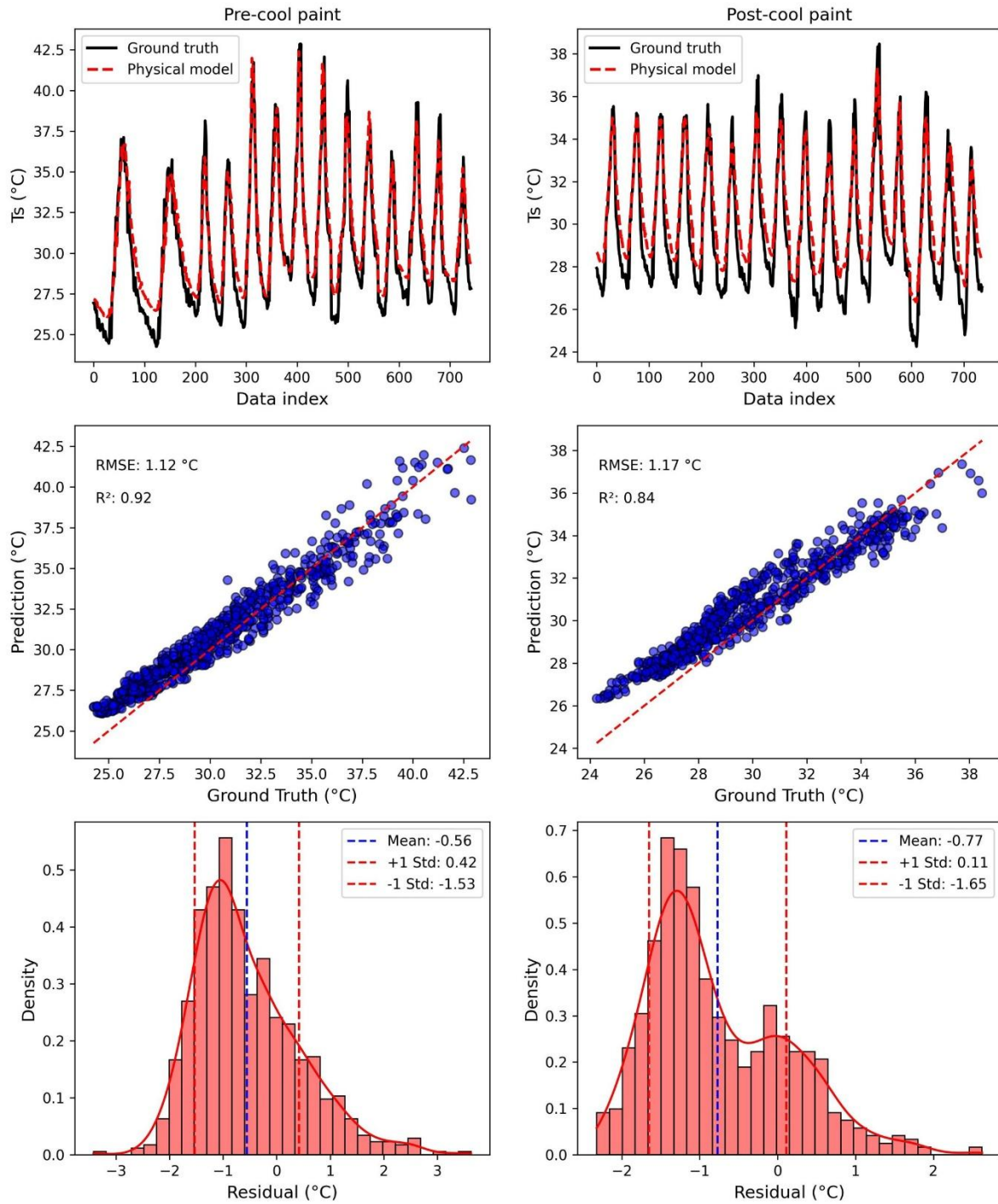


Figure 5: Predicted vertical façade surface temperature by transient physical model

Figure 6 shows the prediction performance of different PIRM. Among the 5 regression models, MLR outperformed the other models in the validation of both pre-cool paint and post-cool paint scenarios. Although XGB performed well, the difference between the training set and validation set scores was larger than MLR indicating the physical model correction may be overfitting.

Predicted vertical façade surface temperature by the optimum physics-informed regression model is illustrated in Figure 7. In the pre-cool paint scenario, physics-informed regression model closely followed the ground truth indicating a strong agreement between the observed and predicted temperatures across the entire temperature range. In the post-cool paint scenario, the model predictions also closely aligned with the ground truth demonstrating the adaptability of physics-informed regression model to changes in the façade's thermal properties after the application of cool paint. The close tracking of the ground truth in both scenarios highlighted the robustness of the physics-informed regression model in predicting façade temperatures under varying surface thermal conditions.

As the scatter plots showed, the points were tightly clustered around the line of $y=x$ for the pre-cool paint condition indicating a high degree of correlation ($R^2 = 0.96$) and a low RMSE of 0.83°C . In contrast, the post-cool paint condition showed a slightly lower correlation ($R^2 = 0.95$) and a lower RMSE of 0.65°C demonstrating that the model still performed well after the paint application. Compared with the physical model, the physics-informed regression model further reduced RMSE by 26% and 44% for pre-cool paint and post-cool paint, respectively.

The density plot of the residuals of the physics-informed regression model showed that the mean residuals for the scenarios pre-cool paint and the post-cool paint were 0.13°C and -0.13°C , respectively. Compared to the physical model, the lower residuals and narrower residual differences for both scenarios suggested that the physics-informed regression model generally maintained a good balance between overestimation and underestimation of temperature predictions.

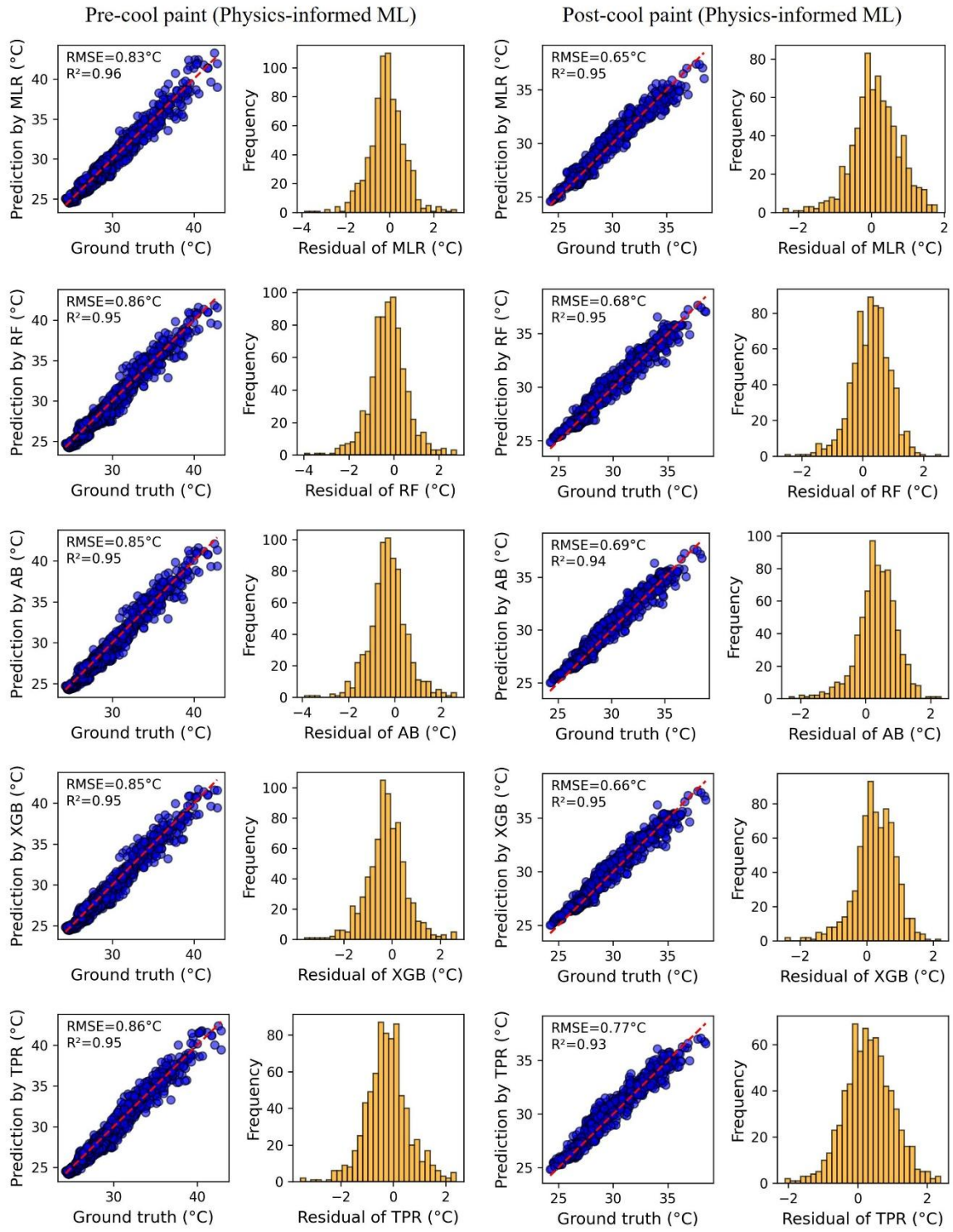


Figure 6: Comparison of prediction performance among PIRM

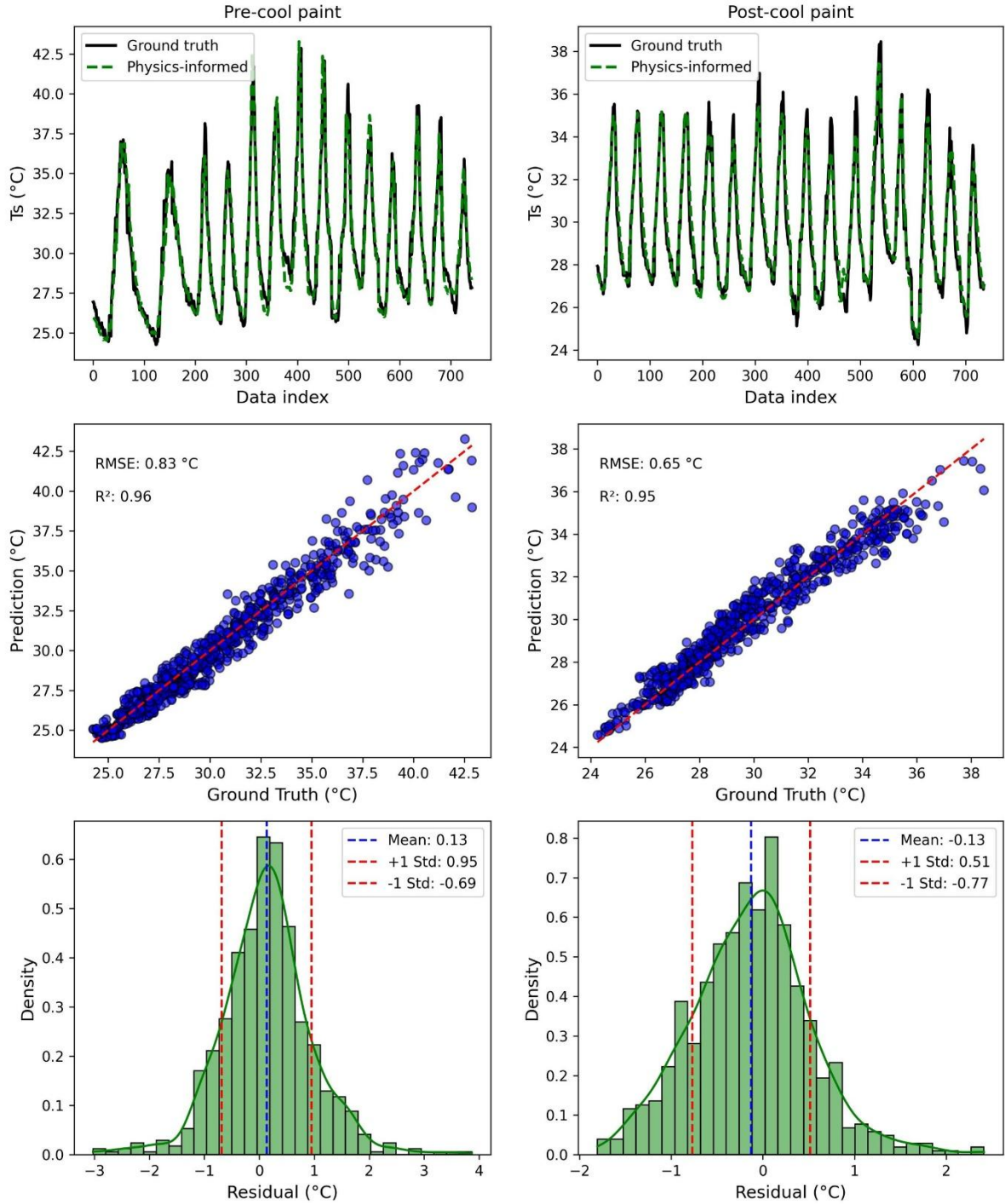


Figure 7: Predicted vertical façade surface temperature by physics-informed regression model (MLR)

3.3 Comparisons of heat flux predictions

In terms of heat flux prediction by physics-informed regression model, the validation of heat flux estimated by unaggregated time series data and hourly average heat flux was showed in Figure 8 and Figure 9, respectively. For the heat flux estimated by unaggregated time series data, the R^2 range from 0.7 to 0.98, with $q_{rad,net}$ scoring the best and q_{net} scored the worst. This discrepancy occurred because

error in the predicted surface temperature was propagated through the heat flux calculations amplifying uncertainties in heat flux components. Consequently, any discrepancy in surface temperature estimation can have a compounding effect on the heat flux prediction, especially for components such as q_{net} aggregating conductive, convective, and radiative heat exchanges. In terms of hourly average heat flux, the q_{conv} for both pre-cool and post-cool paint conditions showed predictions of physics-informed regression model closely tracked the ground truth throughout the day. The q_{conv} ranged from approximately -100 to 25 W/m² for pre-cool paint and from about -60 to 25 W/m² for post-cool paint, reflecting a reduction of approximately 40 W/m² in convective heat losses due to the cool paint. The high R² values (0.97 and 0.94) and relatively low RMSE (7.08 W/m² and 7.02 W/m²) indicate that the model captured the fluctuations in convective heat transfer effectively in both scenarios.

The q_{cond} ranged from about -30 to 10 W/m² for pre-cool paint and from approximately -15 to 10 W/m² for post-cool paint, demonstrating a 15 W/m² cooling in conductive heat transfer due to the cool paint. The q_{cond} had R² values of 0.97 and 0.93, and RMSE of 1.88 W/m² and 1.93 W/m² for pre-cool and post-cool paint, respectively.

The $q_{rad,net}$ was further calculated to examine the heat dynamics related to radiation heat transfer which had values ranging from about -35 to 210 W/m² for pre-cool paint and from approximately -20 to 100 W/m² for post-cool paint. The cool paint provided around 110 W/m² reduction in radiation absorption. The prediction performance was exceptional, with R² values of 1 and 0.98, and RMSE of 4.32 W/m² and 4.30 W/m² for pre-cool and post-cool paint, respectively. The peaks of absorbed radiation and emitted radiation occurred at hour 14-15 and hour 18, respectively.

The q_{net} had values ranging from about -130 to 115 W/m² for pre-cool paint and from approximately -65 to 85 W/m² for post-cool paint, respectively. Solar-reflective material reduced peak q_{net} by approximately 30-65 W/m². The prediction performance was moderate, with R² values of 0.95 and 0.86, and RMSE of 13.24 W/m² and 13.22 W/m² for pre-cool and post-cool paint, respectively. While the model captured the general trend of net heat flux, there was still room for improvement especially after cold paint application.

Comparing the different heat fluxes, it was evident that the $q_{rad,net}$ had the widest range suggesting active heat absorption or release by the radiation heat transfer. The q_{conv} also showed a significant range reflecting the substantial heat transfer between the façade and the surrounding air. The q_{cond} had the smallest range indicating relatively minor heat transfer through the material of the façade compared to the other components.

In terms of hourly average heat transfer dynamics, q_{net} showed a dual role of heat absorption and heat release, with peaks of heat absorption and heat release occurring at hour 13 and hour 17, respectively. $q_{rad,net}$ was mainly positive with peak heat absorption occurring at hour 14-15. The q_{conv} and q_{cond}

were mainly negative reaching a peak at hour 16. The physics-informed regression model could effectively capture these hourly dynamics providing valuable insights into the thermal performance of the facade for both pre-cool paint and post-cool paint scenarios.

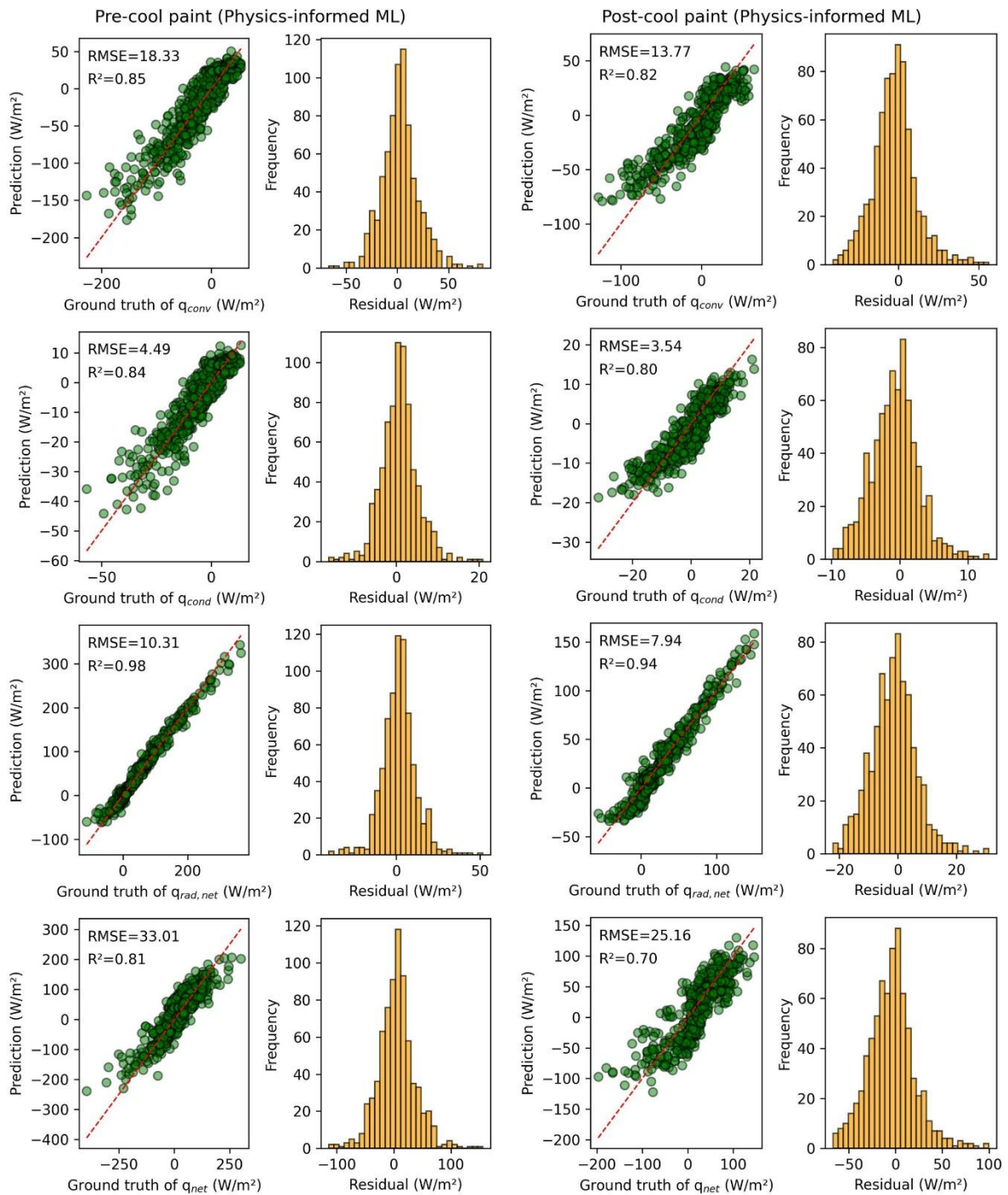


Figure 8: Heat flux estimated by the physics-informed regression model (MLR) using unaggregated time series data

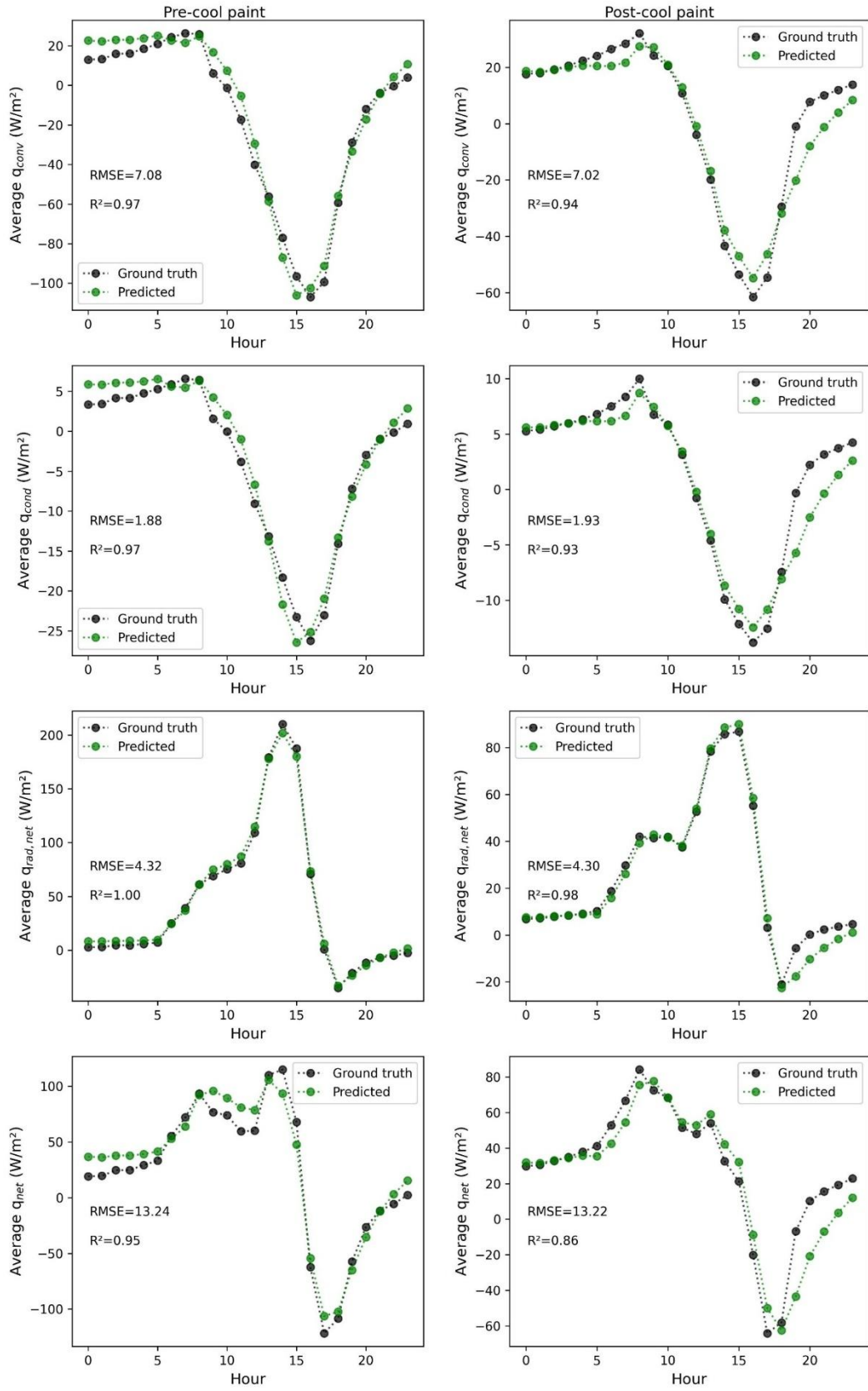


Figure 9: Hourly average heat flux estimated by the physics-informed regression model (MLR)

3.3 Sensitivity analysis of albedo on vertical façade surface temperature

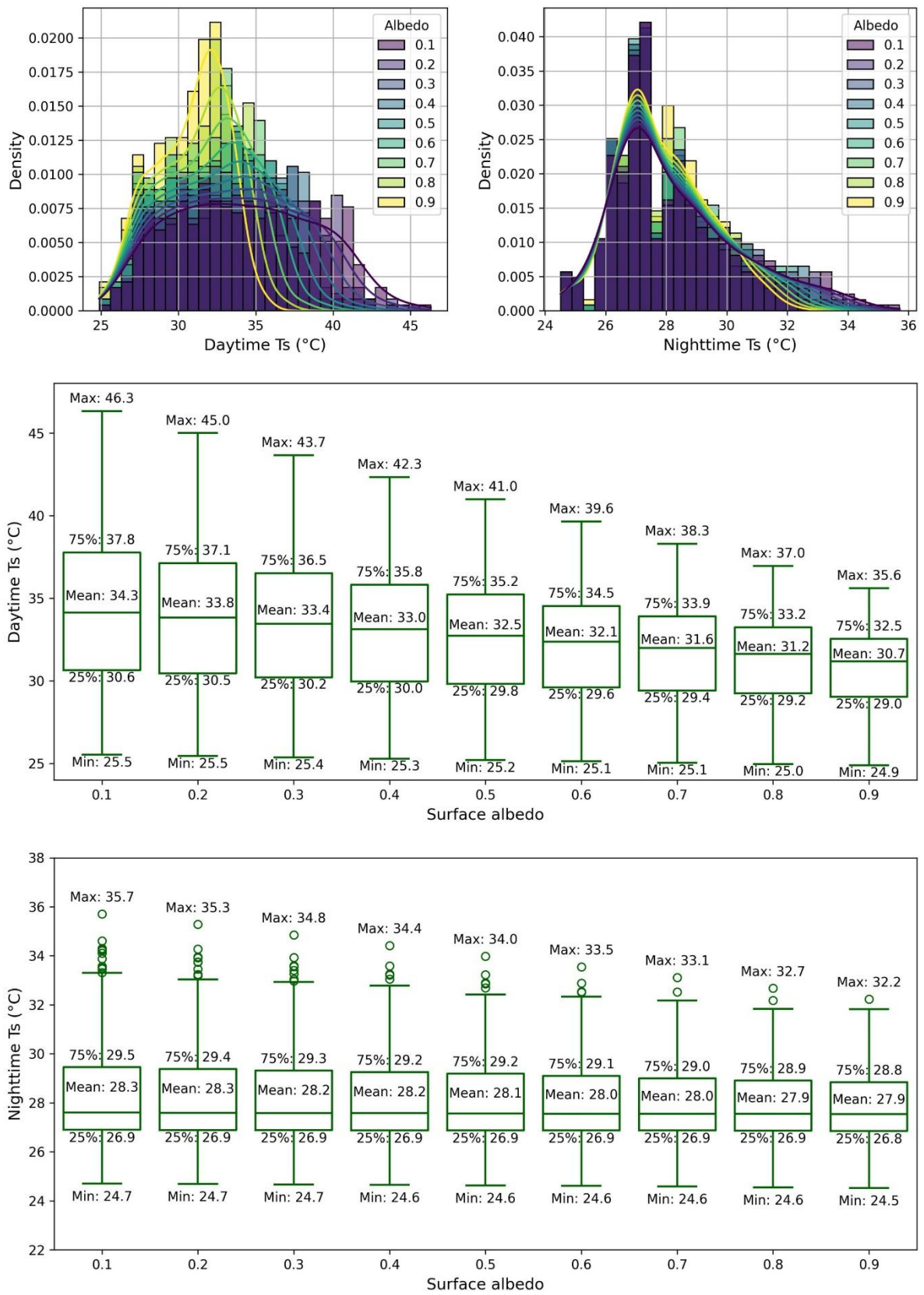


Figure 10: The impact of albedo on vertical façade surface temperature at different periods

The impact of albedo on vertical façade surface temperature is further explored with physics-informed regression model as showed in Figure 10. The daytime histogram reveals a noticeable shift in temperature distribution with changes in albedo. As albedo increases, the peak of the temperature distribution moves to lower temperature. The nighttime histogram shows a less pronounced shift in temperature distribution with changes in albedo compared to the daytime. While there is still a trend towards lower temperatures with higher albedo, the overall impact was much less significant.

The mean daytime temperature decreases as albedo increases. The range of daytime temperatures also narrows with increasing albedo reflecting a more consistent cooling effect across different times of the day for surfaces with higher reflectivity. For instance, the 75th percentile daytime temperature at an albedo of 0.1 is 37.8°C, while the 75th percentile daytime temperature at an albedo of 0.9 is significantly lower at 32.5°C. The cool paint is more effective in mitigating the maximum daytime temperature, which decreases from 46.3°C to 35.6°C when the albedo increases from 0.1 to 0.9. The mean nighttime temperatures decreases with increasing albedo as well, but the difference between the lowest and highest albedo values is less pronounced compared to the daytime.

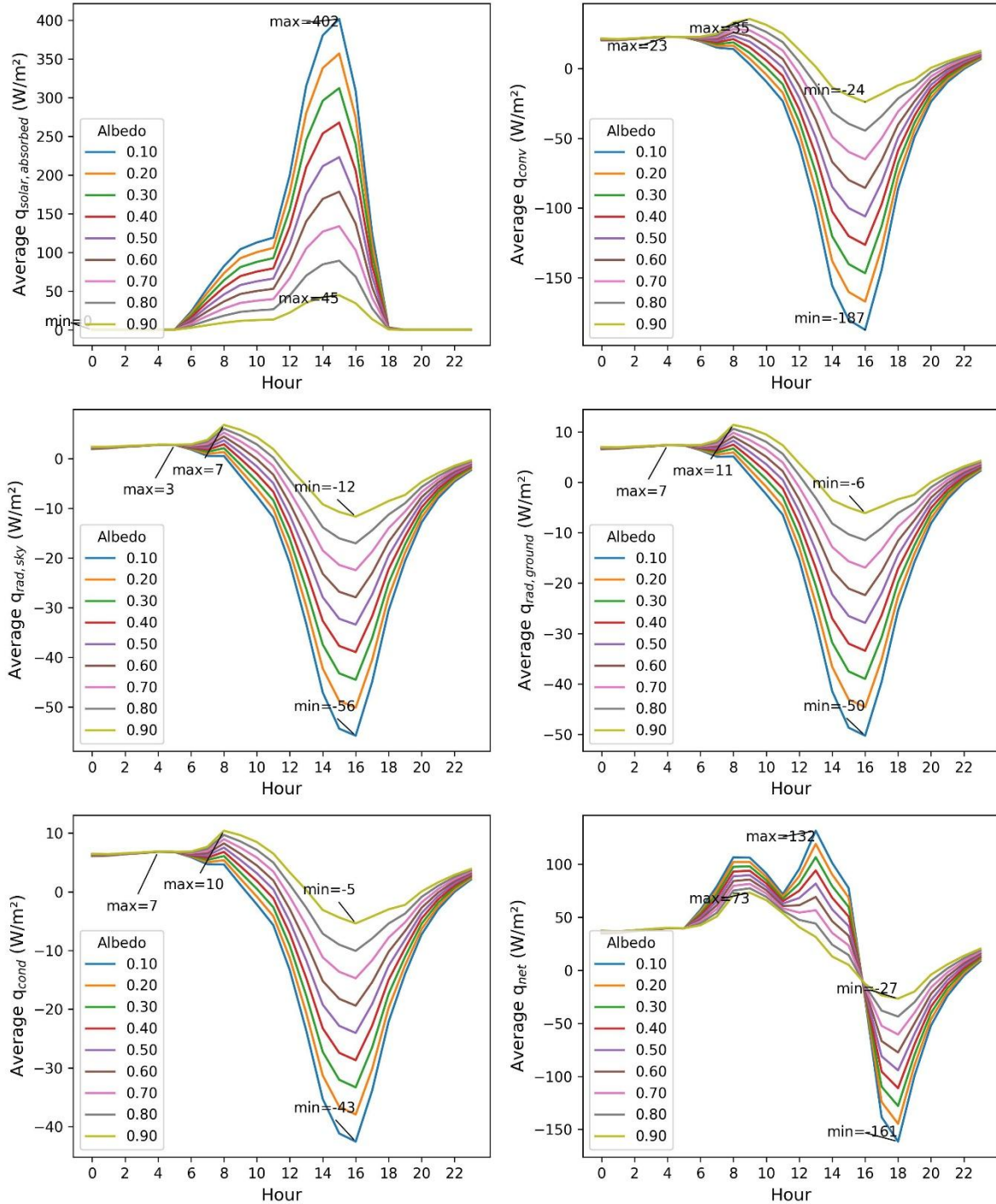


Figure 11: The impact of albedo on heat flux components at different hours

Figure 11 showed that albedo had a significant impact on various heat flux components at different hours of the day. Higher albedo was associated with lower temperatures and thus lower heat transfer through convection, conduction, radiation and energy storage. During peak solar hours, a substantial reduction in heat flux components was observed as the surface albedo increased from 0.1 to 0.9. Absorbed solar radiation ($q_{solar,absorbed}$) reduced significantly from 402 W/m^2 to 45 W/m^2 . Convective heat release (q_{conv}) declined from approximately 187 W/m^2 to 24 W/m^2 . Similarly,

longwave radiative losses to the sky ($q_{rad,sky}$) and ground ($q_{rad,ground}$) decreased from about 56 W/m² to 12 W/m² and from 50 W/m² to 6 W/m², respectively. Conductive heat transfer q_{cond} exhibited a moderate reduction dropping from roughly 43 W/m² to 5 W/m². In addition, the net heat absorbed within the surface layer (q_{net}) decreased significantly from around 132 W/m² to 73 W/m². Subsequently, the net heat release from surface layer (q_{net}) decreased significantly from around 161 W/m² to 27 W/m². These reductions underscore the effectiveness of high-albedo surfaces in minimizing heat absorption and thermal exchange, thereby contributing to improved building energy performance and enhanced indoor thermal comfort.

4. Discussions

4.1 The effectiveness of physics-informed regression modelling

The physics-informed regression modelling demonstrated a competitive advantage versus transient physical modelling as it predicted hourly dynamics of vertical surface temperature with minimal error. This is consistent with previous researches involving thermal and energy modelling of building, where physical simulated data from building energy simulation engine are combined with neural networks to form physics-informed model leveraging the interpretability of building physics models and the predictive power of neural networks [16–18]. In the context of temperature field, the physics-informed deep surrogate model was developed to integrate heat conduction equation and loss function to predict steady-state temperature field of the heat source layout [32]. Among the five investigated regression algorithms, the ordinary least squared based MLR outperformed other nonlinear algorithms in validation dataset. Though XGB was the best estimator in training dataset, its validation performance was not enhanced significantly compared to MLR. This was probably due to that transient physical modelling has resolved most of the nonlinear heat transfer between the building and surroundings as evidenced by a strong agreement in capturing the fluctuations and trends using the transient physical model during periods of higher temperatures and only showed a noticeable deviation from the ground truth in the lower temperature range. Thereby a linear regression can effectively fit the residuals between the ground truths and the predictions. Similar finding was reported in other literature that using physics-informed linear regression in Model Predictive Control (MPC) which outperformed other machine learning methods such as Random Forests and Input Convex Neural Networks [15]. The finding implied that ML methods did not provide competitive advantage over linear regression because it could not find the information provided by physics-based inputs and constraints even though abundant training data was available.

Previous studies on RC materials have largely focused on roof applications [6–9,33,34]. Roof surfaces are horizontal, fully exposed to the sky, and primarily controlled by radiative exchange, with relatively simple and uniform boundary conditions. In tropical applications, RC analysis based on steady-state theoretical framework have established offering the key advantage of resolving wavelength and angle

dependent radiative transfer [8,35,36]. This approach has enabled the determination of minimum material requirements (e.g., 97% solar reflectance, 80% infrared emittance) for achieving sub-ambient temperatures under intense tropical solar irradiance and atmospheric radiation. Because it integrated only the fundamental physics of heat transfer, the formulation was lightweight and fast to solve in tools such as MATLAB once optical spectra were available. However, the calculation assumed steady-state energy balance and was derived for small and horizontal samples neglecting the influence of urban obstructions that modified sky exposure and incident solar irradiance. A previous study reported that when using steady-state equations to estimate temperature of external surface with RC coating, the average error for roof was 49%, while the error for facade was even higher reaching 75% [10]. Other studies have coupled simulation tools to estimate cooling performance of RC materials. One study explicitly incorporated hourly weather data (e.g., solar irradiance, ambient temperature, wind speed, and longwave radiation) into a MATLAB-based thermal model to predict the surface temperature of radiative cooling roofs [34]. The model was then coupled with TRNSYS for building energy simulation under dynamic conditions across three climates. Another study conducted a full-scale RC experiment on the roof of a warehouse, where hourly weather data (e.g., ambient temperature, solar irradiance, wind speed, humidity) were measured and used to validate an EnergyPlus model [7]. The validated model was then applied to simulate annual cooling energy savings under realistic hourly weather conditions in four representative cities.

In contrast, the thermal environment of vertical facades is far more complex, influenced by factors such as variations in the solar incidence angle, shading from nearby buildings, surface reflection, and convective interactions with surrounding airflow. These factors fundamentally alter the balance between radiation, conduction, and convection, rendering roof based steady-state models insufficient to predict the thermal behaviour of facades. The PIRM developed in this study operated in the transient domain, integrating local meteorological data to predict the hourly vertical surface temperature and heat flux on full-scale vertical façades. The approach focused on evaluation of temperature change and heat gain rather than achieving sub-ambient conditions, providing a building-centric framework tailored for practical and building-scale applications and validation. By embedding a machine learning residual corrector within a lumped capacitance energy balance framework, the hybrid model captured onsite discrepancies arising from shading effects, coating aging, sensor bias, or microscale airflow, thereby achieving higher accuracy than purely simulation-based methods. However, this data-driven fidelity requires weeks of calibration with field measurements, and the model needs to be retrained for each new coating formulation or climate environment, which limits its direct transferability.

4.2 The effect of albedo on vertical façade surface temperature

As shown by the sensitivity analysis of changing albedo on vertical façade surface temperature, the daytime temperature reduction with increasing albedo was substantial and expected due to reduced solar reflectance. Since the emissivity of solar reflective materials did not increase, the nighttime temperature

fluctuations with increasing albedo were rather steady compared to the daytime temperatures. Nonetheless, this does not affect the overall energy saving goals of commercial buildings, as air conditioning in commercial buildings mainly operates during daytime hours. In addition, the narrowed daytime temperature distribution and reduction in peak values with increasing albedo implied a more stable thermal behaviour of building with solar-reflective facade. This suggests that solar-reflective material has a thermal buffering effect leading to reduction of heat storage in building materials and improvement of passive cooling during heat waves. The results further show that the reduction in solar radiation absorption has a ripple effect through all heat transfers such as convection, radiation, conduction, and energy storage. Typical radiative cooling material can generate average daily cooling power up to 100 W/m² [9]. In this research, direct $q_{solar,absorbed}$ reduces significantly from 402 W/m² to 45 W/m² and the predicted net heat release from q_{net} will decrease significantly from around 161 W/m² to 27 W/m² as albedo increases from 0.1 to 0.9. This implies that solar-reflective material not only reduces surface temperatures but also reduces the heat fluxes affecting indoor comfort and air conditioning load. This is critical for UHI mitigation as stored and released heat is a major driver of UHI intensity in the urban environment.

Compared to black-box machine learning model, the underlying physical laws of the proposed model are useful in identifying the key transient heat transfers showing superior advantages in model interpretability, while interpretable machine learning methods such as partial dependence plots [37] or accumulated local effects [38] can only decode the relationship between input variables and output variable.

4.3 Practical implications and limitations

Singapore plans to use solar-reflective paint on all government-sold residential blocks by 2030 to mitigate urban heatwaves [39]. The proposed model can be adopted for pre-evaluation of heat mitigation effects of solar-reflective material especially for surface temperature and net heat fluxes data, which can be used as input for urban energy simulations at the city scale. The hybrid modelling framework developed in this research is generalizable to different regions and climatic contexts (e.g., temperate climate or subtropical climate). By embedding physical laws within machine learning, the model can be retrained or fine-tuned with few local environmental data. This kind of transfer learning is valuable for urban planners and building designers seeking to optimize passive cooling strategies across diverse climate zones.

In terms of limitations, simplifying assumptions are applied in the physical modelling of the internal wall temperature and the ground surface temperature, which may lead to inaccurate estimation of the conductive and radiative heat fluxes (e.g., $q_{rad,ground}$). The calculations of sky emissivity and air convective heat transfer coefficient are based on empirical equations and require proper validation and calibration when used in other regions and climate conditions. Directly estimating the heat flux

components should reduce discrepancies in heat flux calculations due to error propagation in surface temperature estimation. In addition, current model focused on clear sky and high solar irradiance conditions to ensure stable boundary conditions for model training and validation. Rainy and cloudy periods were excluded due to their strong transient effects and measurement uncertainties that may obscure the physical relationships between solar input and surface response. Nonetheless, it is acknowledged that tropical climate was also characterized by frequent rainfall and high humidity. The developed PIRM should be further expanded to predict surface temperatures under rainy and cloudy weather conditions in the future to enhance its practical applicability.

5. Conclusions

The standalone transient physical model overestimated the vertical façade surface temperature especially in lower temperature range for both pre-cool paint ($R^2=0.92$, $RMSE=1.12^\circ C$) and post-cool paint ($R^2=0.84$, $RMSE=1.17^\circ C$) scenarios. The physics-informed MLR model demonstrated high prediction accuracy in predicting vertical facade temperature for pre-cool paint ($R^2=0.96$, $RMSE=0.83^\circ C$) and post-cool paint ($R^2=0.95$, $RMSE=0.65^\circ C$) scenarios, outperformed other machine learning algorithms such as RF, AB, XGB and TPR. Compared to the standalone transient physical model, the physics-informed regression approach reduced RMSE by 26% and 44% for pre-cool paint and post-cool paint, respectively.

The physics-informed regression model based on MLR effectively captured the hourly average heat fluxes across both pre-cool and post-cool paint scenarios ($R^2=0.86-1$). q_{net} ($R^2 = 0.86-0.95$, $RMSE=13.22-13.24$ W/m²) had values ranging from about -130 to 115 W/m² for pre-cool paint and from approximately -65 to 85 W/m² for post-cool paint, respectively. Solar-reflective material reduced peak q_{net} by approximately 30-65 W/m². The q_{net} showed peak heat gain around hour 13 and peak heat loss around hour 17. The $q_{rad,net}$ remained mostly positive with maximum heat absorption between hour 14 and 15. Both q_{conv} and q_{cond} were predominantly negative peaking in magnitude at hour 16.

As albedo increases from 0.1 to 0.9, surface temperature and associated heat fluxes decline significantly. The 75th percentile daytime temperature reduces from 37.8°C to 32.5°C and the maximum daytime temperature reduces from 46.3°C to 35.6°C when the albedo increases from 0.1 to 0.9. The associated $q_{solar,absorbed}$ drops from 402 W/m² to 45 W/m² and the net heat release from q_{net} decreases significantly from around 161 W/m² to 27 W/m². These results highlight that solar-reflective material is effective in modulating the surface temperature and thereby supporting better building energy efficiency and enhanced indoor thermal comfort.

Conflicts of Interest: The authors declare no conflict of interest.

Acknowledgements

This research was supported by: (1) Supporting Cooling NUS with Baseline-Evaluating-Action-Monitoring (BEAM) initiative from National University of Singapore; (2) The Fujian Province Young and Middle-aged Teacher Education and Research Project Funding (JAT241009) (3) The Open Fund of Key Laboratory of Ecology and Energy Saving Research of Dense Habitat, Ministry of Education (20240105); (4) Fuzhou University Research Starting Fund (511470); (5) Fuzhou University Testing Fund of Precious Apparatus (2025T031).

Appendix A: Calibration of IR camera

In this study, we used a FLIR A50 Smart Camera with a 95° field of view to measure concrete wall surface temperature. Camera settings were adjusted accordingly to measure the surfaces with emissivity of 0.95. The camera was installed on the rooftop of the nearby low-rise building SDE3, approximately 75 m from the target wall. Although the camera was calibrated before rooftop installation, the protective casing with a crystal glass window in front of the lens may introduce measurement errors due to reflections.

To assess this effect, we borrowed another IR camera of the same model, newly calibrated, and placed it on tripod adjacent to the housed SDE3 IR camera on the rooftop (Figure A1). The borrowed IR camera was factory-calibrated and further calibrated in laboratory using a handheld portable infrared calibrator (CEM BX-500).



Figure A1: Site photos of calibration on rooftop using a calibrated camera on the left for the installed IR camera on the right.

As shown in Figure A2, the calibrated IR camera reported surface temperatures 5°C–8°C lower than the housed SDE3 IR camera across various surfaces. The differences for the unpainted and painted concrete

walls were 6.5°C and 7°C, respectively, indicating the necessity of temperature calibration for the SDE3 IR camera used for long-term monitoring.

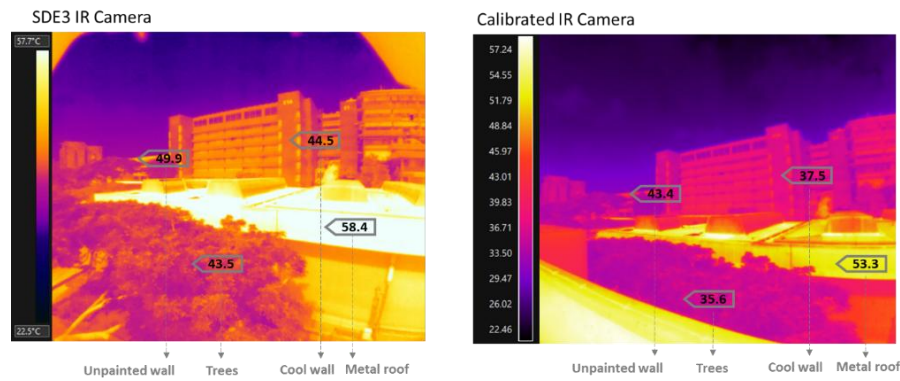


Figure A2: Thermal images taken by the side-by-side IR cameras at the same timing.

During a 3-day calibration experiment, wall surface temperatures were measured simultaneously during daytime by the calibrated IR camera, existing SDE3 rooftop IR camera, and thermocouple. Both IR camera captured thermal images at 2-minute intervals, while the thermocouple recorded at 1-minute intervals. As shown in Figure A3, the thermocouple measurements align well with those of the calibrated IR camera, and both are consistently lower than the readings from the housed SDE 3 IR camera.

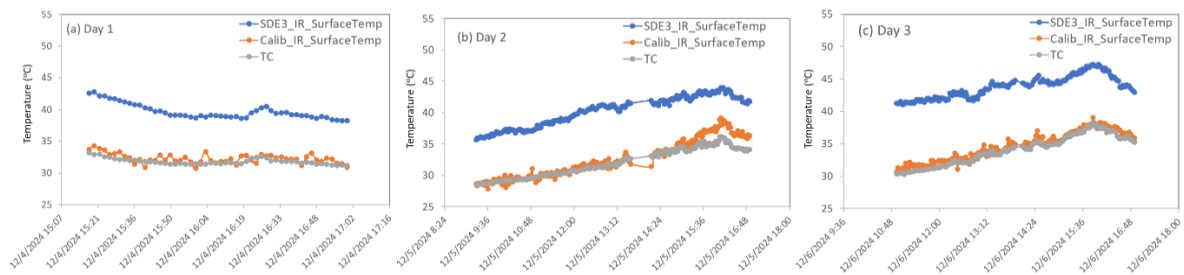


Figure A3: Comparison of surface temperatures captured by different equipment for three days.

Correlations were developed between temperatures measured by the SDE3 IR camera and those obtained from the other two methods using the 3-day dataset (Figure A4). The correlation between the SDE3 IR camera and the thermocouple exhibited a higher R^2 than that with the calibrated IR camera, which showed slightly greater fluctuations. Therefore, the thermocouple data are taken as the reference for calibrating the SDE3 IR camera.

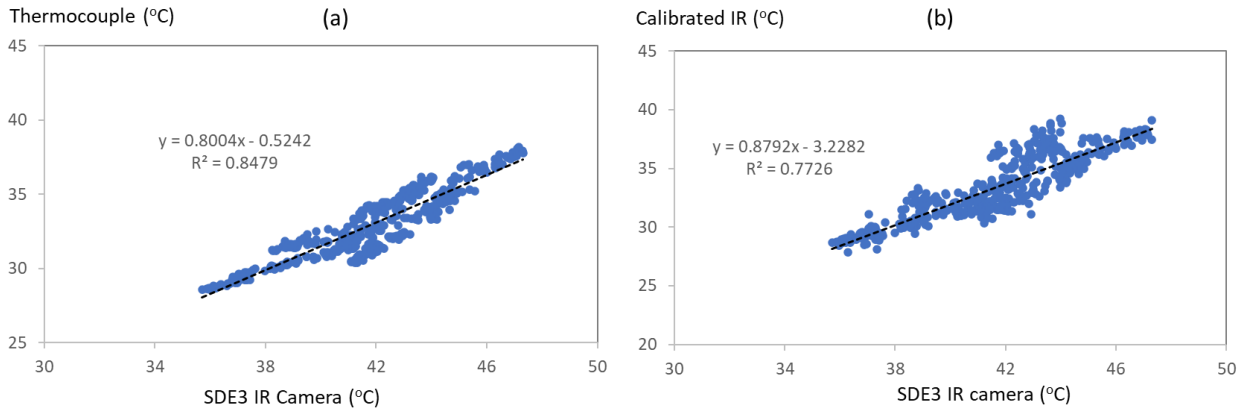


Figure A4: Correlation between the surface temperatures measured by different methods.

Based on the analysis, we assumed the thermocouple measurement to be accurate and used the correlation in Figure A4 (a) to calibrate the surface temperatures measured by the existing SDE3 IR camera.

References

1. Building and Construction Authority. Green Mark 2021 Technical Guide. 2021;1–36.
2. Li W, Li Y, Shah KW. A materials perspective on radiative cooling structures for buildings. *Sol Energy*. 2020;207(April):247–69.
3. Chen L, Zhang K, Ma M, Tang S, Li F, Niu X. Sub-ambient radiative cooling and its application in buildings. *Build Simul*. 2020;13(6):1165–89.
4. Yan T, Xu D, Meng J, Xu X, Yu Z, Wu H. A review of radiative sky cooling technology and its application in building systems. *Renew Energy*. 2024;220(November 2023).
5. Pirvaram A, Talebzadeh N, Leung SN, O'Brien PG. Radiative cooling for buildings: A review of techno-enviro-economics and life-cycle assessment methods. *Renew Sustain Energy Rev*. 2022;162(March).
6. Chen J, Lin K, Pan A, Zhu Y, Chung Ho T, Gong Q, et al. Innovating building energy regulations enabled by radiative sky cooling: Enhanced code of practice for overall thermal transfer value (OTTV) of super-cool roofs. *Energy Convers Manag*. 2024;306(December 2023).
7. Wang N, Lv Y, Zhao D, Zhao W, Xu J, Yang R. Performance evaluation of radiative cooling for commercial-scale warehouse. *Mater Today Energy*. 2022;24.
8. Hanif M, Mahlia TMI, Zare A, Saksahdan TJ, Metselaar HSC. Potential energy savings by radiative cooling system for a building in tropical climate. *Renew Sustain Energy Rev*. 2014;32:642–50.
9. Li H, Zhang K, Shi Z, Jiang K, Wu B, Ye P. Cooling benefit of implementing radiative cooling on a city-scale. *Renew Energy*. 2023;212(April):372–81.
10. Wang S, Yang L, Liu Y, Pang J, Yang L, Dou M. Full-scale experimental study of the surface cooling effect of prefabricated buildings utilizing passive radiative cooling under real operating conditions. *Energy*. 2025;328(April).
11. Karniadakis GE, Kevrekidis IG, Lu L, Perdikaris P, Wang S, Yang L. Physics-informed machine learning. *Nat Rev Phys*. 2021;3(6):422–40.
12. Wang R, Kashinath K, Mustafa M, Albert A, Yu R. Towards Physics-informed Deep Learning for Turbulent Flow Prediction. *Proc ACM SIGKDD Int Conf Knowl Discov Data Min*. 2020;1457–66.
13. Sharma P, Chung WT, Akoush B, Ihme M. A Review of Physics-Informed Machine Learning in Fluid Mechanics. *Energies*. 2023;16(5):1–21.
14. Wang X, Dong B. Physics-informed hierarchical data-driven predictive control for building HVAC systems to achieve energy and health nexus. *Energy Build*. 2023;291(January).
15. Bünning F, Huber B, Schalbetter A, AbouDonia A, Hudoba M, Badyn D, et al. Physics-informed linear regression is competitive with two Machine Learning methods in residential building MPC. 2022;310.
16. Gokhale G, Claessens B, Develder C. Physics informed neural networks for control oriented thermal modeling of buildings. *Appl Energy*. 2022;314(March).
17. Chen Y, Yang Q, Chen Z, Yan C, Zeng S, Dai M. Physics-informed neural networks for building thermal modeling and demand response control. *Build Environ*. 2023;234(November 2022).
18. Ma Z, Jiang G, Chen J. Physics-informed ensemble learning with residual modeling for enhanced building energy prediction. *Energy Build*. 2024;323(September).

19. Chen L, Fang B, Zhao L, Zang Y, Liu W, Chen Y, et al. DeepUrbanDownscale: A physics informed deep learning framework for high-resolution urban surface temperature estimation via 3D point clouds. *Int J Appl Earth Obs Geoinf*. 2022;106.
20. Yang F, Ding W, Zhao J, Song L, Yang D, Li X. Rapid Urban Flood Inundation Forecasting Using a Physics-Informed Deep Learning Approach. *Ssrn*. 2024;
21. Kashinath K, Mustafa M, Albert A, Wu JL, Jiang C, Esmaeilzadeh S, et al. Physics-informed machine learning: Case studies for weather and climate modelling. *Philos Trans R Soc A Math Phys Eng Sci*. 2021;379(2194).
22. Osczevski RJ. The Basis of Wind Chill. *Arctic*. 1995;48(4):372–82.
23. Khabari A, Zenouzi M, O'Connor T, Rodas A. Natural and forced convective heat transfer analysis of nanostructured surface. *Lect Notes Eng Comput Sci*. 2014;1:317–9.
24. Perovic B, Klimenta D, Jevtic M, Milovanović M, Perović B, Jevtić M. the Effect of Different Sky Temperature Models on the Accuracy in the Estimation of the Performance of a Photovoltaic Module. *J Tech Univ Gabrovo*. 2019;59(November):78–82.
25. Hong J, Michael Utzinger D. Reducing the Heat Island Effect: A Mathematical Model of Green Roof Design. *Build Simul Conf Proc*. 2022;1279–86.
26. Martin M, PBerdahl A. Characteristics of infrared sky radiation in the United States. *Sol Energy*. 1983;33(3–4):321–36.
27. Python Software Foundation. Python 3.9.19 documentation. 2024.
28. Pedregosa F, Varoquaux G, Gramfort A, Michel V, Thirion B, Grisel O, et al. Scikit-learn: Machine learning in Python. *J Mach Learn Res*. 2011;
29. Chen T, He T, Benesty M. XGBoost : eXtreme Gradient Boosting. *R Packag version 071-2*. 2024;1–4.
30. Hollmann N, Müller S, Purucker L, Krishnakumar A, Körfer M, Hoo S Bin, et al. Accurate predictions on small data with a tabular foundation model. *Nature*. 2025;637(8045):319–26.
31. Chen S, Wong NH, Ignatius M, Zhang W, He Y, Yu Z, et al. ATLAS: Software for analysing the relationship between urban microclimate and urban morphology in a tropical city. *Build Environ* [Internet]. 2022;208(September):108591. Available from: <https://doi.org/10.1016/j.buildenv.2021.108591>
32. Zhao X, Gong Z, Zhang Y, Yao W, Chen X. Physics-informed convolutional neural networks for temperature field prediction of heat source layout without labeled data. *Eng Appl Artif Intell*. 2023;117(September 2022).
33. Guo L, Liang Z, Li W, Yang C, Wang E. The Review of Radiative Cooling Technology Applied to Building Roof—A Bibliometric Analysis. *Sustain*. 2024;16(16):1–20.
34. Feng J, Saliari M, Gao K, Santamouris M. On the cooling energy conservation potential of super cool roofs. *Energy Build*. 2022;264.
35. Han D, Fei J, Mandal J, Liu Z, Li H, Raman AP. Sub-ambient radiative cooling under tropical climate using highly reflective polymeric coating. *Sol Energy Mater Sol Cells*. 2022;240(March):1–9.
36. Han D, Fei J, Li H, Ng BF. The criteria to achieving sub-ambient radiative cooling and its limits in tropical daytime. *Build Environ*. 2022;221(May):1–9.
37. Hastie T, Tibshirani R, Friedman J. *The Elements of Statistical Learning: Data Mining, Inference, and Prediction*. 2nd ed. New York: Springer; 2009.

38. Apley DW, Zhu J. Visualizing the effects of predictor variables in black box supervised learning models. *J R Stat Soc Ser B Stat Methodol.* 2020;82(4):1059–86.
39. Jacob C. All HDB estates to use heat-reflective paint to mitigate urban heat [Internet]. 2025. Available from: <https://www.channelnewsasia.com/singapore/hdb-green-towns-programme-cool-coatings-paint-all-estates-urban-heat-4912396>